Adaptive Frequency Responsive Control for Wind Farm Considering Wake Interaction

Xue Lyu, Youwei Jia, and Zhaoyang Dong

***Abstract*—With the increasing share of wind power, it is expected that wind turbines would provide frequency regulation ancillary service. However, the complex wake effect intensifies the difficulty in controlling wind turbines and evaluating the frequency regulation potential from the wind farm. We propose a novel frequency control scheme for doubly-fed induction generator (DFIG)-based wind turbines, in which the wake effect is considered. The proposed control scheme is developed by incorporating the virtual inertia control and primary frequency control in a holistic way. To facilitate frequency regulation in time-varying operation status, the control gains are adaptively adjusted according to wind turbine operation status in the proposed controller. Besides, different kinds of power reserve control approaches are explicitly investigated. Finally, extensive case studies are conducted and simulation results verify that the frequency behavior is significantly improved via the proposed control scheme.**

***Index Terms*—Doubly-fed induction generator (DFIG)-based wind turbine, virtual inertia control, primary frequency control, power reserve control, wake interaction.**

NOMENCLATURE

λ	Tip speed ratio
ρ	Air density
β	Pitch angle
ω_r	Rotor speed
ω_{r0}	Wind turbine (WT) rotor speed at the beginning of inertial response
ω_{r1}	WT rotor speed at time t_1
$\omega_{r,\min}$	The minimum WT rotor speed
$\omega_{r,\max}$	The maximum WT rotor speed
ω_{rnom}	Nominal WT speed
$\omega_{ropt}(\beta=\theta)$	Optimal rotor speed under a certain pitch angle θ
ω_{rove}	Accelerated rotor speed to achieve the required deloading level
ω_s	Rotor speed of synchronous generators SGs
ω_{s0}	SG rotor speed at the beginning of inertial response
ω_{s1}	SG rotor speed at time t_1
$\Delta\omega_r$	WT rotor speed variation
$\Delta\omega_s$	SG rotor speed variation
δv_i	Aggregated wind deficit of the i^{th} WT
δv_{ij}	Velocity deficit of the i^{th} WT generated by the upstream j^{th} WT
A_i	Area swept by rotor blades
A^{shadow}	Area of WT under shadowing
$A_{j\to i}^{shadow}$	Overlap between the area spanned by the wake shadow cone generated by the j^{th} WT and the area swept by the i^{th} WT
C_p	Power coefficient
C_{pdel}	Power coefficient in the deloading mode
C_T	Thrust coefficient
D_j	Diameter of the j^{th} WT blades
d_{ij}	Distance between the center of the i^{th} downstream WT and the center of the wake effect generated by the j^{th} upstream WT
E	Kinetic energy stored in the rotational rotor
f	System frequency
f_{nom}	Nominal frequency
Δf	Frequency deviation
H	Inertia constant
H_{vir}	Virtual inertia coefficient of WT
J	WT equivalent inertia
J_{tur}	Turbine inertia
J_{gen}	Generator inertia
k	Decay constant
K_d	Droop gain
K_{in}	Inertia coefficient
K_{in0}	Virtual inertia coefficient when WT operates at $\omega_{r,\max}$
L_{ij}	Distance between the center of wake effect and the shadow area
n	Gear-box ratio
$P_{act}(t_0)$	Actual power output of WT at time t_0
P_{del}	Captured wind power in deloading mode

Manuscript received: April 15, 2020; accepted: September 17, 2020. Date of CrossCheck: September 17, 2020. Date of online publication: February 9, 2021.

This work was partially supported by Natural Science Foundation of China (No. 72071100), Guangdong Basic and Applied Basic Research Fund (No. 2019A1515111173), Department of Education of Guangdong Province, and Young Talent Program (No. 2018KQNCX223).

X. Lyu and Y. Jia (corresponding author) are with the Department of Electrical and Electronic Engineering, Southern University of Science and Technology, Shenzhen, China, and X. Lyu is also with the Department of Electrical and Electronic Engineering, The University of Hong Kong, Hong Kong, China (e-mail: xuelu111@gmail.com; jiayw@sustech.edu.cn).

Z. Dong is with School of Electrical Engineering and Telecommunications, The University of New South Wales, Sidney, Australia (e-mail: joe.dong@unsw.edu.au).

DOI: 10.35833/MPCE.2020.000237

P_{mpp}	The maximum captured wind power
P_{nom}	WT nominal power
P_{ref}	Active power reference of WT
P_w	Mechanical power captured by WT
ΔP	Deviation between the mechanical power and electrical power of SGs
ΔP_d	Power support provided by the droop control
ΔP_d^{pri}	WT primary reserve
ΔP_{in}	Power support provided by the virtual inertia control
R	Rotor blade radius
v	Wind speed
v_0	Free wind speed
v_{rated}	Rated wind speed
$x_i - x_j$	Distance from the j^{th} WT and the i^{th} WT along with the wind direction

I. Introduction

In recent years, variable speed wind turbines (WTs), i.e., the doubly-fed induction generator (DFIG)-based WTs, the permanent-magnet synchronous generator (PMSG)-based WTs, are widely utilized due to their merits of high-energy conversion efficiency [1]. However, WTs connect to the main grid through power electronic devices, which makes them loosely coupled with system frequency. In addition, they have no primary reserve due to the maximum power point tracking (MPPT) control. Currently, with the increasing penetration of wind energy in modern power system, there is a rising interest that wind farms (WFs) should provide frequency regulation support. Due to the intermittent and fast changing nature of wind speed, it is challenging to control the overall wind power output in a frequency-responsive way. The control complexity can be even entangled by considering the intrinsic wake effect.

To ensure power system stability, the basic requirement is to maintain the instantaneous balance between the generation and demand. Once the imbalance occurs, the subsequent frequency behavior will be immediately subject to the overall system inertia, and then can be remedied by frequency-responsive units [2]. Recently, some researchers find that the kinetic energy (KE) stored in the rotational rotor of WT can be utilized as an energy buffer to provide rapid-yet-temporary active power support. This kind of control strategy is generally referred as virtual inertial control [3], [4], which aims to restrain the rate of change of frequency (RoCoF). In [5], a proportional relationship between the electrical torque of WTs and the RoCoF is constructed. Considering that the fixed gain may not contribute satisfactory inertial response in practical operation due to the ambient wind speed fluctuation, a fuzzy control strategy is proposed in [6] to dynamically regulate the inertia gain. To avoid the destabilization of WTs induced by KE discharging, a large-perturbation nonlinear WT model is proposed in [7] and the virtual inertia gain is tuned according to the wind speed. A dynamic droop-based inertial control is designed in [8], in which a shaping function about the droop gain and the RoCoF is developed. Intuitively, this virtual inertia control by temporarily utilizing KE is capacity-constrained. To further provide a relatively long frequency regulation support, wind power curtailment or deloading shall be employed to obtain a sufficient amount of primary reserve. In terms of different physical reactions of WTs, the primary reserve can be obtained via adjusting rotor speed, blade pitch angle and their combinations [9]-[12]. In general, the pitch angle control is usually less desirable as its frequent manipulation might lead to irreversible fatigue of WTs. Therefore, a conventional cascaded control is widely adopted. For example, the rotor speed control is used at low wind speed to perform deloading operation and the pitch adjustment action only activates at high wind speed [13], [14]. In contrast, a non-zero-pitch-angle-based control strategy is proposed in [15], and simulation results demonstrate that this strategy can also effectively protect the pitch servo from tear-and-wear and adequately exploit the KE buffer during dynamic operation. After obtaining a certain amount of primary reserve, WTs can participate in the primary frequency control. In order to enable WTs to support frequency regulation of the power grid, a dynamic droop controller based on fuzzy logic is designed in [16].

Considering WF level, individual WTs that are collectively committed to frequency regulation should not neglect the naturally existing wake effect. Conventionally, the aggregated WT model is widely adopted in existing works, where aerodynamic interactions among WTs are not considered. Obviously, such simplification cannot evaluate the frequency regulation capability of a WF accurately. By far, researches on frequency responsive control of WTs with detailed wake model is still at its infant stage. The impact of wake effect on the WF inertial capacity is quantified in [17], and simulation results indicate that the overall inertial contribution is significantly reduced by wake effect. Considering the non-negligible wake effect and the time-varying operation status of WTs, the inertia gain in [18] is adjusted according to the available KE storage capacity to improve frequency nadir. To determine the optimal profile of wind power extraction throughout the overproduction process via KE discharging, a heuristic control strategy is proposed in [19], where the wind speed difference experienced by individual WTs is considered. To enable the WF to trace the dispatch command given by the system operator, active power regulation tasks are assigned to WTs according to KE charging/discharging range in [20]. In [21] and [22], different operation strategies of WFs, e.g., maximize total KE, maximize overall wind power generation, maximize total KE while deloading WF at a certain level, are developed. Although the optimal cooperation among WTs can be achieved by solving optimization problems, a high computation burden exists with high complexity involved in WT model and wake model. In addition, the time-varying characteristic of wind speeds and load demands intensifies the difficulty in achieving online control.

To instantly provide adequate frequency regulation support from multiple WTs, we propose an adaptive frequency responsive control scheme, where the wake interactions are fully considered. The main contributions of this paper are as follows.

1) The proposed control scheme incorporates the virtual inertia control and primary frequency control in a holistic way, so that the RoCoF and the frequency deviation can be

effectively mitigated.

2) The control gains in the designed controller are adaptively adjusted, which guarantees that the frequency control performance for WTs with different operation status can be matched with their frequency regulation capabilities.

3) To investigate the impacts of wake interactions on the frequency regulation contribution and total power production from WF, different approaches of power reserve control are explicitly investigated.

The remainder of this paper is organized as follows. The WT model and wake model are introduced in Section II. The proposed control framework for WTs participating in frequency regulation is presented in Section III. The simulation results and the relevant discussions are given in Section IV. Finally, Section V concludes this paper and presents the further work.

II. WT Model and Wake Effect Model

A. WT Model

The system configuration of DFIG-based WT is depicted in Fig. 1, which comprises a WT, gear box, induction generator and back-to-back converter. It can be observed that the stator is directly interfaced with the power grid, while the rotor is connected to the power grid through a back-to-back converter. In general, the capacity of the back-to-back converter is about 20%-30% of WT nominal capacity. Specifically, the rotor-side converter (RSC) controls the desired active power reference of WT. The grid-side converter (GSC) controls the stability of DC-link voltage. The details of the generator and converter model can be referred to [23].

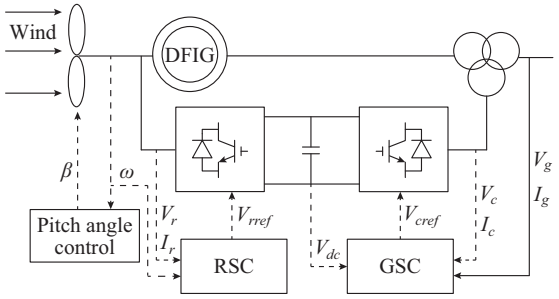

Fig. 1. Schematic diagram of DFIG-based WT.

The mechanical power extracted from wind P_w is defined as:

$$P_w = \frac{1}{2}\rho\pi R^2 v^3 C_p(\lambda,\beta) \tag{1}$$

C_p indicates a nonlinear relationship between the tip speed ratio and pitch angle. According to [24], C_p can be formulated as:

$$C_p = 0.22\left(\frac{116}{\lambda_i} - 0.4\beta - 5\right)\mathrm{e}^{-\frac{12.5}{\lambda_i}} \tag{2}$$

$$\frac{1}{\lambda_i} = \frac{1}{\lambda + 0.08\beta} - \frac{0.035}{\beta^3 + 1} \tag{3}$$

$$\lambda = \frac{\omega_r R}{v} \tag{4}$$

The pitch angle maintains at zero degree in case that wind speed is lower than the rated value. C_p is only correlated with λ. According to (1)-(4), there exists an optimal rotor speed that yields the maximal power coefficient $C_{p,\max}$ for a given wind speed. To ensure the maximum power capture, the active power reference of WT for a measured rotor speed can be calculated as:

$$P_{mpp} = \begin{cases} \dfrac{\rho}{2}\pi R^2 C_p(\lambda_{opt,\beta=0},0)v^3 & v \le v_{rated} \\ P_{nom} & v > v_{rated} \end{cases} \tag{5}$$

Once the wind speed is larger than the rated value, the pitch angle control would be activated to maintain the power output of the WT at the nominal value.

B. DFIG Model and Converter Model

Considering the fast response of the converter, the flux dynamics are neglected and the generator is modelled as a controlled current source. Specifically, the decoupled active current and the excitation current determine the active and reactive power injected to the power grid, respectively. The RSCs and GSCs are self-commutated converters. RSC operates in a stator-flux *dq*-reference frame, in which the rotor current is decomposed into an active power (*q*-axis) component and a reactive power (*d*-axis) component. A cascaded control structure is utilized. The fast inner loop controls the reactive and active components of the rotor current and the slower outer loop regulates the reactive and active power to determine current set-points. GSC operates in an AC-voltage *dq*-reference system. Similarly, a cascaded control structure is designed, and the inner loop is the same with that of the rotor side control. The outer loop controls the DC-link voltage to determine the *q*-axis current set-point.

C. Wake Effect Model

WTs extract the energy from the wind, and the wind leaving the turbine has a lower energy compared with the case when it reaches in front of the turbine, which is known as wake effect. The total power production of WF is influenced by the aggregated wake effect. To estimate the reduction of wind power generation, several wake effect models have been proposed since 1980s [25]. Different wake effect models are compared in [26], and no particular difference of the accuracy exists between the sophisticated models and simplified models. Due to the relatively simple model and the fairly acceptable accuracy, the Jensen's wake model has been one of the most prevalent models for engineering applications [27]. It is established based on the assumption that wake expands linearly towards downstream, as shown in Fig. 2. The downstream WT of wind speed can be given by:

$$v_i = v_0(1 - \delta v_i) \tag{6}$$

Note that wind speed reaching the i^{th} WT is affected by not only the upstream WT which is directly in front of it, but also other upstream WTs. The aggregated velocity deficit of the i^{th} WT is expressed as:

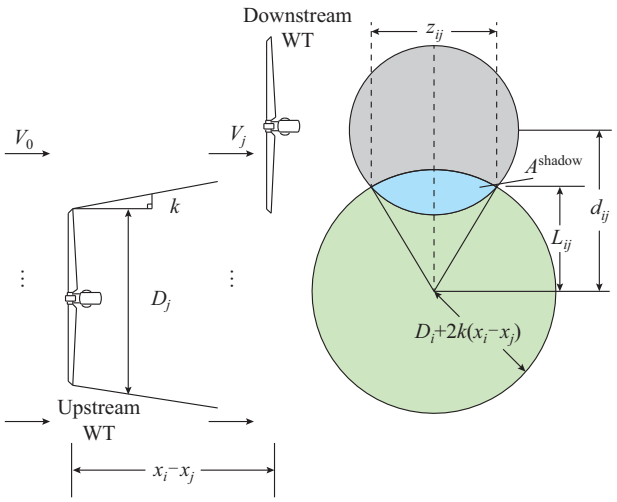

Fig. 2. Jensen's wake effect model.

$$\delta v_i = \sqrt{\sum_{j\in N: x_j<x_i} (\delta v_{ij})^2} \tag{7}$$

$$\delta v_{ij} = \left(1-\sqrt{1-C_{Tj}}\right)\left[\frac{D_j}{D_j+2k(x_i-x_j)}\right]^2 \frac{A_{j\to i}^{shadow}}{A_i} \tag{8}$$

The thrust coefficient also indicates a nonlinear relationship between tip speed ratio and pitch angle, and it can be obtained through look-up table or curve fitting, as given in Fig. 3. $A_{j\to i}^{shadow}$ can be expressed as follows. A detailed example of the shadow area is shown in Fig. 2.

$$A_{j\to i}^{shadow} = [D_i+2k(x_i-x_j)]^2 \cos^{-1}\left(\frac{L_{ij}}{D_i+2k(x_i-x_j)}\right) + D_i^2\cos^{-1}\left(\frac{d_{ij}-L_{ij}}{D_i+2k(x_i-x_j)}\right) - d_{ij}z_{ij} \tag{9}$$

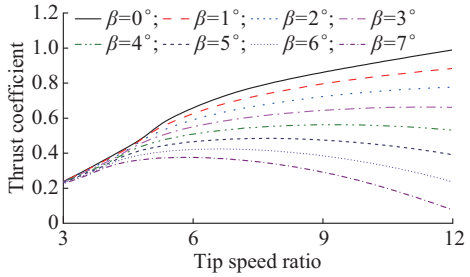

Fig. 3. Thrust coefficient.

III. Proposed Control Scheme

In the proposed control scheme, the virtual inertia control and primary frequency control are essentially integrated, as shown in Fig. 4. Under a certain deloading operation condition, in case of under-frequency events occur, each WT releases the stored KE and the primary reserve to offer frequency regulation support. In case over-frequency events occur, to counterbalance frequency variation, KE can be charged and the deloading level of WTs can be increased until the allowable limit is reached. Specifically, the virtual inertia gain and the droop gain are adaptively adjusted according to rotor speed and primary reserve capacity of WTs. The online tuned control gains guarantee the good matching effect between the frequency regulation from individual WTs and their available frequency regulation capability.

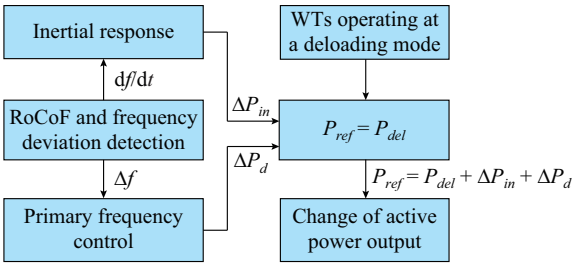

Fig. 4. Proposed coordinated frequency control scheme.

A. Virtual Inertia Control

System inertia provides sufficient time for synchronous generators (SGs) to re-establish power balance, which reflects the capability of power system to restrain RoCoF. For SGs, their rotor speed is locked to the system frequency apart from transient conditions when the load angle is varying. Once the supply-demand imbalance occurs, the mechanical inertia of SGs can be intrinsically utilized to mitigate frequency fluctuation. This dynamic process can be expressed as:

$$\Delta P = 2H\omega_s \frac{\mathrm{d}\omega_s}{\mathrm{d}t} = 2Hf\frac{\mathrm{d}f}{\mathrm{d}t} \tag{10}$$

As the mechanical rotor speed of DFIG-based WT is decoupled from system frequency, it has no intrinsic inertia from the system aspect. However, with the introduction of an appropriate additional control loop, WT can also contribute inertial response.

For an individual DFIG-based WT, KE stored in its rotational rotor can be expressed as:

$$E = \frac{1}{2}J\omega_r^2 = \frac{1}{2}\left(\frac{J_{tur}}{n^2}+J_{gen}\right)\omega_r^2 \tag{11}$$

The electric power in the form of KE charging/discharging variation can be calculated by taking the derivative of (11), which yields:

$$\Delta P_{in} = \frac{\mathrm{d}E}{\mathrm{d}t} = J\omega_r\frac{\mathrm{d}\omega_r}{\mathrm{d}t} \tag{12}$$

The inertia constant of WT is defined as:

$$H = \frac{J\omega_{rnom}^2}{2P_{nom}} \tag{13}$$

Based on the definition of inertia constant, (12) can be rewritten as (14) in per-unit form:

$$\Delta P_{in} = 2H\omega_r\frac{\mathrm{d}\omega_r}{\mathrm{d}t} \tag{14}$$

Analogous to SG, we define H_{vir} as the virtual inertia coefficient of WT, and (14) can further be rewritten as:

$$\Delta P_{in} = 2H\omega_r\frac{\mathrm{d}\omega_r}{\mathrm{d}t} = 2H_{vir}\omega_s\frac{\mathrm{d}\omega_s}{\mathrm{d}t} \tag{15}$$

Integrating (15) over time t_0 to t_1, we can obtain:

$$\int_{t_0}^{t_1} 2H\omega_r\,\mathrm{d}\omega_r = \int_{t_0}^{t_1} 2H_{vir}\omega_s\,\mathrm{d}\omega_s \tag{16}$$

$$H(\omega_{r1}^2-\omega_{r0}^2)=H_{vir}(\omega_{s1}^2-\omega_{s0}^2) \tag{17}$$

Rearranging (17), the virtual inertia coefficient can be defined as:

$$H_{vir}=\frac{\Delta\omega_r(2\omega_{r0}+\Delta\omega_r)}{\Delta\omega_s(2\omega_{s0}+\Delta\omega_s)}H \tag{18}$$

In particular, $\Delta\omega_r=\omega_{r1}-\omega_{r0}$, and $\Delta\omega_s=\omega_{s1}-\omega_{s0}$. Substituting H_{vir} with H, ΔP_{in} can be rewritten as:

$$\Delta P_{in}=2H\frac{\Delta\omega_r(2\omega_{r0}+\Delta\omega_r)}{\Delta\omega_s(2\omega_{s0}+\Delta\omega_s)}\omega_s\frac{\mathrm{d}\omega_s}{\mathrm{d}t} \tag{19}$$

Normally, $2\omega_{r0}>>\Delta\omega_r$ and $2\omega_{s0}>>\Delta\omega_s$, which leads to:

$$\Delta P_{in}=2H\frac{\omega_{r0}\Delta\omega_r}{\omega_{s0}\Delta\omega_s}\omega_s\frac{\mathrm{d}\omega_s}{\mathrm{d}t} \tag{20}$$

As mentioned above, SG rotor speed is locked to system frequency. Hence, (20) can be rewritten as:

$$\Delta P_{in}=2\left(\frac{\omega_{r0}}{f_0}K_{in}H\right)f\frac{\mathrm{d}f}{\mathrm{d}t} \tag{21}$$

KE stored in the rotating mass of WTs can be utilized to smooth against frequency fluctuation. It can be observed from (21) that the virtual inertial response depends on the rotor speed at the beginning of the inertial response ω_{r0} and the virtual inertia coefficient K_{in}. In order to obtain the inertial support transformed from KE variation, the controller needs to "remember" ω_{r0}, which can be achieved by using a simple sample and hold module. In general, once the power imbalance disturbance occurs, the larger K_{in} is, the larger inertial support can be provided. However, there are practical limits on virtual inertia coefficient, and the potential risk of instability would bring along if such limits are overcome. For example, the excessive rotor speed deceleration may lead to the shut-down of WTs. To adequately utilize KE to contribute inertial response while maintain the stability of WT in varying wind speed environment, K_{in} is designed to be adaptively adjusted according to the available rotor speed variation range:

$$K_{in}=\begin{cases}K_{in0}\dfrac{\omega_r(t_0)-\omega_{r,\min}}{\omega_{r,\max}-\omega_{r,\min}} & f<1\\ K_{in0}\dfrac{\omega_{r,\max}-\omega_r(t_0)}{\omega_{r,\max}-\omega_{r,\min}} & f>1\end{cases} \tag{22}$$

Figure 5 shows the block diagram of the proposed virtual inertia controller. A first-order low-pass filter is introduced to omit the measurement noise from RoCoF. An amplitude limiting step is set to ensure that K_{in} varies between [0, $K_{in}^{\max}$].

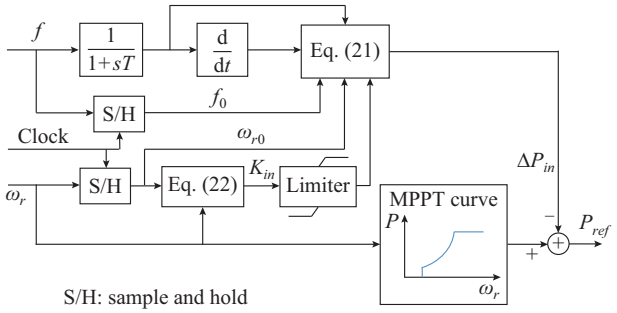

Fig. 5. Block diagram of virtual inertia control.

B. Primary Frequency Control

1) Different Primary Reserve Approaches

The regular operation mode for WTs is based on the widely-used MPPT strategy, where the blade pitch angle maintains at zero degree and the active power reference is generated via the MPPT curve for a given measured rotor speed, as shown in Fig. 5. To join in system primary frequency control, WTs are supposed to provide a relatively long period of active power support. However, this is infeasible for WTs in the MPPT operation mode. Admittedly, a deloading control is essential to offer a primary reserve margin.

The primary reserve can be effectually obtained by shifting the maximum power point (MPP) towards another point with a lower power coefficient. With a certain wind speed, for individual WTs, the deloading point can be located at point *B* (as shown in Fig. 6) via the zero-pitch-angle-based deloading control, where the redundant power can be stored as KE. Alternatively, adjusting the blade pitch angle can also achieve power curtailment. For example, the WT can operate at point *C* via the non-zero-pitch-angle-based deloading control. The blade pitch angle increases to a certain value and the rotor speed varies to another value, i. e., $\omega_{ropt}(\beta>0°)$, which ensures the maximum power capture with the pitch angle.

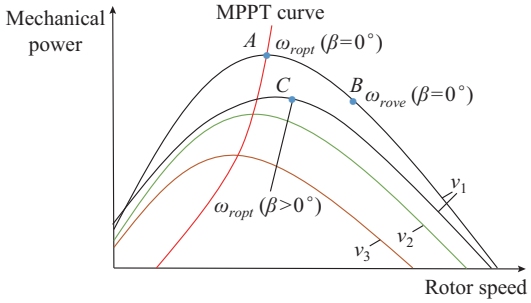

Fig. 6. Different deloading approaches for WTs.

The power extracted from wind in the deloading mode, i.e., P_{del}, can be expressed as:

$$P_{del}=\frac{1}{2}\rho\pi R^2C_{pdel}v^3 \tag{23}$$

For the zero-pitch-angle-based deloading control, the deloading principle is to accelerate rotor speed while maintaining the blade pitch angle at zero degree. The mechanical power output can be expressed as:

$$P_{del}=\frac{1}{2}\rho AC_{pdel}\left(\frac{\omega_{rove}R}{v},\beta=0°\right)v^3 \tag{24}$$

Based on (24), once P_{del} is determined, the corresponding ω_{rove} can be determined. Correspondingly, a new rotor speed versus active power reference curve can be obtained. The previous MPPT curve has to be bypassed by the new deloading curve. It should be noted that rotor speed control is subject to the physical constraint. Once the rotor speed reaches to its upper limit, i.e., $\omega_{r,\max}$, the pitch angle control would be activated.

For the non-zero-pitch-angle-based deloading control, like point *C* in Fig. 5, the deloading principle is achieved by inte-

grating the pitch angle based regulation and the rotor speed based regulation. The mechanical power output of a WT can be expressed as:

$$P_{del}=\frac{1}{2}\rho A C_{pdel}\left(\frac{\omega_{ropt}(\beta=\theta)R}{v},\beta=\theta\right)v^3 \tag{25}$$

Similarly, once the deloading requirement is determined, the corresponding pitch angle θ and rotor speed $\omega_{ropt}(\beta=\theta)$ can be determined. As a result, a new rotor speed versus active power reference curve can be obtained. To implement non-zero-pitch-angle-based deloading control, the offset pitch angle θ should be added to pitch angle controller besides the replacement of original MPPT curve.

For individual WTs, utilizing the zero-pitch-angle-based deloading control can enhance the storage capacity of KE. However, considering the internal wake interactions in a WF, utilizing the zero-pitch-angle-based deloading control for all WTs may no longer be the optimal solution. As shown in Fig. 3, when adopting the zero-pitch-angle-based deloading control, the thrust coefficient of WTs increases and the wind speed imposing down-WTs would decrease due to wake effect. In contrast, when the non-zero-pitch-angle-based deloading control is adopted, the wind speed deficit decreases and in turn the total wind production loss would be reduced. Therefore, owning to the mutual effect amongst up-stream and down-stream WTs, the selection of primary reserve control approaches would significantly affect the total storage capacity of KE and wind power production from WF.

2) Droop Control

The deloading level is predefined in accordance with a coefficient d_1 in normal operation. With the primary power reserve, the output power of WT can be regulated upward or downward to counterbalance the frequency variation. In response to under-frequency events, the active power support provided by WTs is bounded by the primary power reserve d_1P_{mpp}. In contrast, when the over-frequency disturbances occur, the active power support provided by WT is bounded by the allowable deloading level d_2.

Analogous to SGs, a droop control for WT is tailored as:

$$\Delta P_d=K_d(f-f_{nom}) \tag{26}$$

According to (26), a large droop gain setting brings about significant primary frequency regulation and vice versa. As reported in [28], the steam driven turbines equipped with the electro-hydraulic governors typically have a droop parameter $1/K_d$ setting in a range of 2.5%-8%. The droop setting is in a range of 0%-10% for hydro-turbines. In this paper, to encourage WTs to contribute a large share of primary frequency response, the droop parameter is set to be 2.5% when the mechanical power output of WT reaches to the nominal value, i. e., $R_0=2.5\%$. Apparently, the fixed droop gain setting would inevitably result in the mismatch between K_d and frequency regulation capability when wind speed varies. To dynamically adjust the droop gain in response to the changing working conditions, the droop gain is set to be proportional to the available primary reserve of WT ΔP_d^{pri}:

$$K_d\propto\Delta P_d^{pri} \tag{27}$$

For a given wind speed, the maximum mechanical power output of WT can be calculated according to (5). And then the primary reserve ΔP_d^{pri} can be determined as:

$$\Delta P_d^{pri}=\begin{cases}P_{mpp}(t)-P_{act}(t_0) & f\le 1\\ P_{act}(t_0)-d_2P_{mpp}(t) & f>1\end{cases} \tag{28}$$

Rewriting (27) and (28), the droop coefficient can be dynamically adjusted as:

$$K_d=\begin{cases}\dfrac{1}{R_0}\dfrac{P_{mpp}(t)-P_{act}(t_0)}{d_1P_{nom}} & f<1\\ \dfrac{1}{R_0}\dfrac{P_{act}(t_0)-d_2P_{mpp}(t)}{d_1P_{nom}} & f>1\end{cases} \tag{29}$$

Figure 7 shows the block diagram of the proposed primary frequency control. It can be found that for WTs adopting the zero-pitch-angle-based deloading control, the primary frequency support ΔP_d is directly sent to the original active power reference generation model to obtain the new active power reference. For WTs adopting the non-zero-pitch-angle based deloading control, ΔP_d is also sent to the pitch controller to generate the pitch angle compensation value via a PI controller. An amplitude limiting step is set to guarantee the droop gain K_d varying between [0, $K_d^{\max}$]. In addition, the upper limit of ΔP_d is subjected to the maximum mechanical power output. And the lower limit of ΔP_d is subjected to the allowable deloading level of WT, i. e., $[P_{act}(t_0)-P_{mpp}(t), P_{act}(t_0)-d_2P_{mpp}(t)]$.

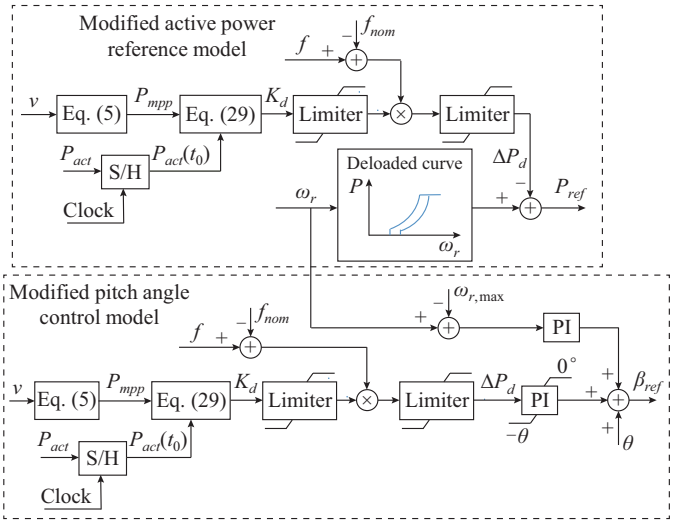

Fig. 7. Block diagram of primary frequency control.

IV. Case Studies

A. Experiment Setup

A test system comprising two SGs, two constant power loads, and a DFIG-WT based WF is developed in DIgSILENT/PowerFactory, which is shown in Fig. 8. The aggregated WT model is not used in this paper. In contrast, each WT is modeled in detail and the experienced wind speed is calculated according to the wake equations (6) - (9). A WF with 8 identical DFIG-WTs is studied, and the nominal capacity for each WT is 5 MW. The WF layout has two paral-

lel strings and each string has four WTs, which is shown in Fig. 7. These two parallel strings are connected to a 30 kV collector bus. There is an equal space between the neighboring WTs, i.e., 5D, and each WT is connected to the collector system via a 6.25 MVA, 0.69 kV/3.3 kV/30 kV transformer. L_1 represents a fixed load $PL_1+\mathrm{j}QL_1$, i.e., 120 MW + 4 Mvar. L_2 represents a dump load to emulate sudden load increase/decrease events, i.e., 15 MW + 1 Mvar. Detailed simulation parameter settings are referred to Appendix A.

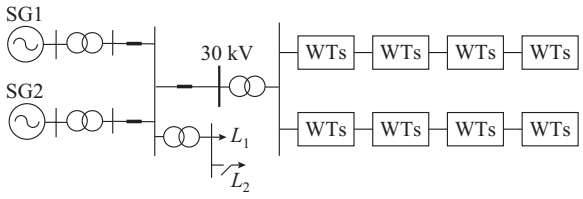

Fig. 8. Configuration of test system.

The deloading level of each WT is set to be 10% in the normal operation, and the maximum allowable deloading level of each WT is set to be 30% when over-frequency event occurs to test the proposed control strategy. As illustrated in Section III, applying different primary reserve approaches would influence the total storage capacity of KE and wind power generation. To assess the impacts of high complex wake interactions on overall frequency regulation and power production from WF, four deloading schemes are developed.

1) The zero-pitch-angle-based deloading control is applied to all WTs.

2) The first-row WTs employ the non-zero-pitch-angle-based deloading control. Meanwhile, the rest WTs utilize zero-pitch-angle-based deloading control.

3) The first-row and the second-row WTs employ the non-zero-pitch-angle-based deloading control while the rest ones adopt the zero-pitch-angle-based deloading control.

4) The first-row, second-row and third-row WTs employ the non-zero-pitch-angle-based deloading control and the last-row WTs adopt zero-pitch-angle-based deloading control.

B. Sudden Load Increase with Constant Wind Speed

To generate an under-frequency event, a sudden load increase is introduced to the testing system by switching L_2 on at $t=30$ s. The concerned free wind speed is $v_0=10$ m/s. The simulation results with MPPT control, the proposed control with different deloading schemes, and the scenario without considering wake effect are compared in Fig. 9. It is revealed from Fig. 9(a) that the frequency nadir is 49.398 Hz and the quasi-steady state frequency is 49.779 Hz through MPPT control when the load disturbance occurs. As indicated in Fig. 9(a), when the proposed control is implemented, the frequency nadir and steady-state frequency are both significantly improved. Specifically, the frequency nadir increases to 49.620 Hz, 49.599 Hz, 49.580 Hz and 49.566 Hz via the proposed control with deloading scheme 1, 2, 3 and 4, respectively. And the corresponding quasi-steady state frequency increases to 49.806 Hz, 49.799 Hz, 49.794 Hz, and 49.791 Hz, respectively. It reveals that the potential of frequency nadir increase is proportional to the total KE storage. Meanwhile, the decrease of quasi-steady state frequency deviation is proportional to the capacity of primary power reserve. Obviously, the implementation of zero-pitch-angle-based deloading control can enhance the total storage capacity of KE in normal operation. As a result, the improvement of the frequency nadir is most significant with deloading scheme 1. On the other hand, the non-zero-pitch-angle-based deloading control can decrease the wind power production loss in normal operation. According to Fig. 9(b), prior to load disturbance, the power production of WF is 11.526 MW, 11.958 MW, 12.318 MW, and 12.512 MW, with the implementation of deloading schemes 1, 2, 3 and 4, respectively. This is because the manipulation of pitch angle of upstream WTs can increase the wind velocity experienced by downstream WTs. In the situation where the wake interactions are ignored and all WTs are assumed to experience the free wind speed, the deloading scheme 1 is the optimal approach as it can store the most amount of KE and reduce the manipulation frequency of blade pitch angle as much as possible. In this context, the frequency nadir increases to 49.662 Hz and the quasi-steady state frequency increases to 49.806 Hz after load disturbance. As indicated in Fig. 9(a) and (b), the overall wind power production and frequency regulation capability from WF would be both over-estimated without considering wake effect.

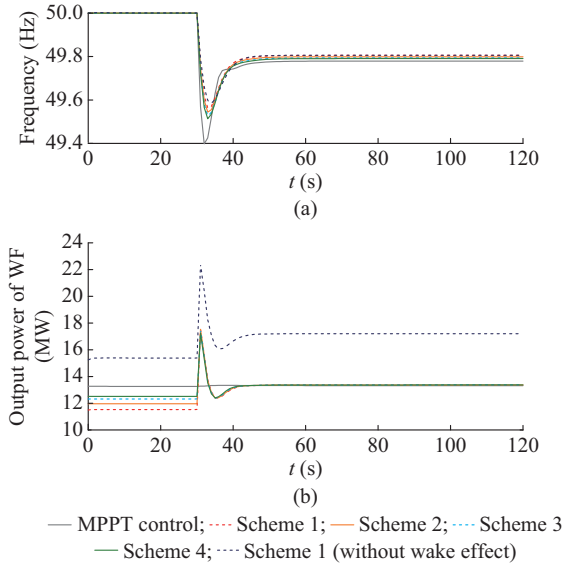

Fig. 9. Simulation results during under-frequency event. (a) System frequency. (b) Output power of WF.

C. Sudden Load Decrease with Constant Wind Speed

To generate an over-frequency event, a sudden load increase is introduced in the test system by switching L_2 off at $t=30$ s. Figure 10 shows the results for $v_0=10$ m/s. It is revealed from Fig. 10(a) that the frequency peak is 50.597 Hz and the quasi-steady state frequency is 50.221 Hz through MPPT control. The proposed control with deloading schemes 1, 2, 3 and 4 is implemented. The frequency peak decreases to 50.441 Hz, 50.431 Hz, 50.415 Hz, and 50.408 Hz, and the corresponding quasi-steady state frequency de-

creases to 50.205 Hz, 50.198 Hz, 50.193 Hz and 50.188 Hz, respectively. In contrast to the under-frequency event, simulation results reveal that the decrease of frequency peak is proportional to the charging range of KE and the decrease of frequency deviation is proportional to the available deloading margin. As shown in Fig. 10(c) and (d), when the load event of sudden decrease occurs, to provide frequency regulation support, the rotor speed of all WTs is accelerated to the upper limit. Pitch angle control is activated until the deloading level reaches the predefined limit. In the situation where wake effect is not considered, in case of sudden load decreases, the frequency peak decreases to 50.454 Hz and the quasi-steady state frequency decreases to 50.173 Hz with the implementation of the proposed control with deloading scheme 1. As the available charging range of KE is small in this case, the decrease of frequency peak is not significant. Nevertheless, the decrease of quasi-steady-state frequency deviation is still over-estimated compared with the situation when the wake effect is considered.

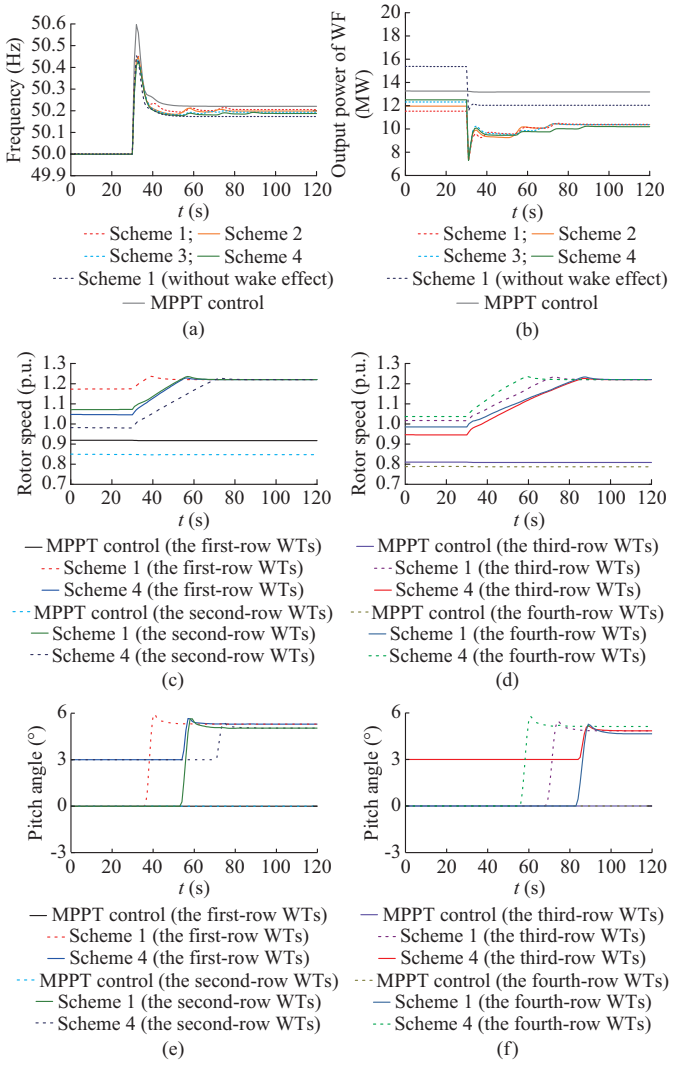

Fig. 10. Simulation results during over-frequency event. (a) System frequency. (b) Output power of WF. (c) Rotor speed of DFIG for the first-row and second-row WTs. (d) Rotor speed of DFIG for the third-row and fourth-row WTs. (e) Pitch angle of DFIG for the first-row and second-row WTs. (f) Pitch angle of DFIG for the third-row and fourth-row WTs.

D. Frequency Response with Time-varying Wind Speed

A set of fluctuated wind speed data for 320 s is captured to verify the proposed control. As shown in Fig. 11(a), compared with conventional MPPT control, the dynamic frequency behavior of the system is remarkably improved by means of the proposed control schemes.

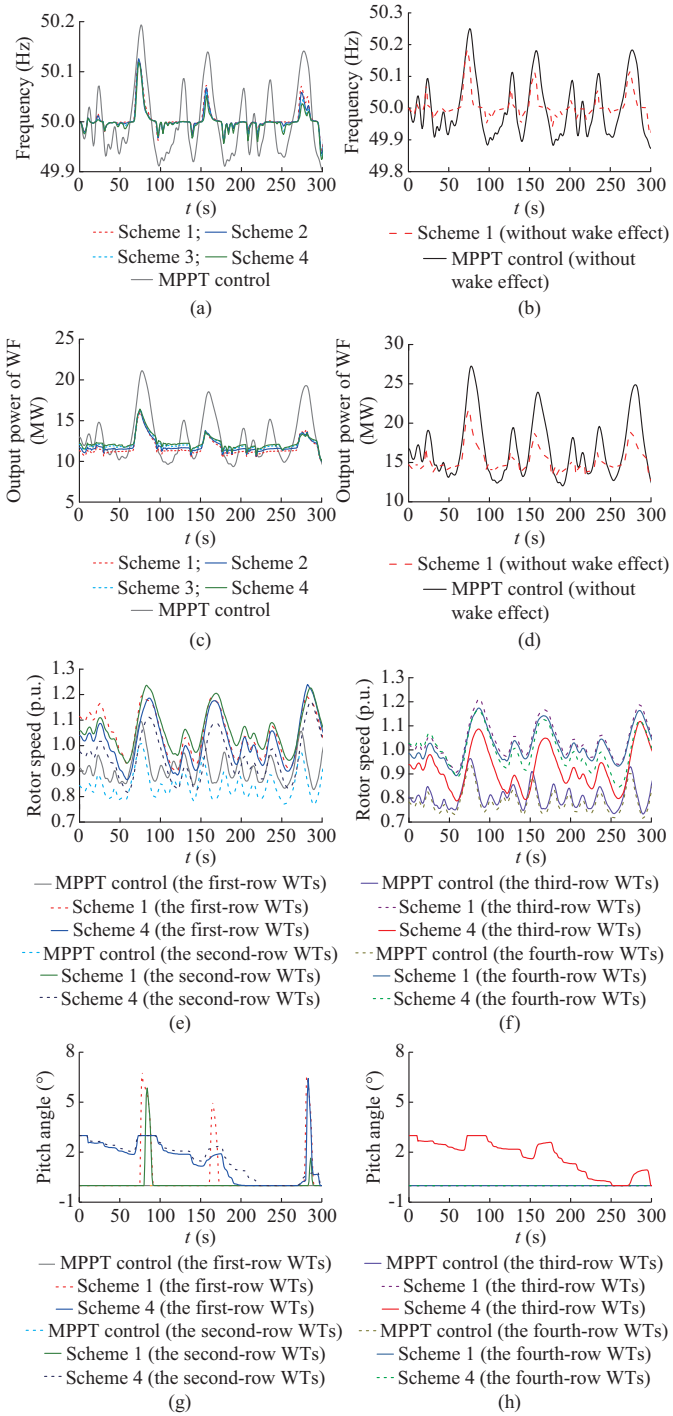

Fig. 11. Simulation results under time-varying wind speed condition. (a) System frequency. (b) System frequency without wake effect. (c) Output power of WF. (d) Output power of WF without wake effect. (e) Rotor speed of DFIG for the first-row and second-row WTs. (f) Rotor speed of DFIG for the third-row and fourth-row WTs. (g) Pitch angle of DFIG for the first-row and second-row WTs. (h) Pitch angle of DFIG for the third-row and fourth-row WTs.

To make a quantitative comparison, the standard deviation of system frequency throughout 320 s is calculated with the sampling time of 1 s. It can be found that the standard deviation of frequency is 0.0673 throughout the simulation by means of MPPT control. In the case where the proposed coordinated control with deloading schemes 1, 2, 3 and 4 is implemented, respectively, the frequency deviation decreases to 0.0249, 0.0233, 0.0223, and 0.0217, respectively. As verified in previous subsections, the zero-pitch-angle-based deloading control has a better performance in under-frequency event and non-zero-pitch-angle-based deloading control has a better performance in over-frequency event. The overall over-frequency disturbance is more severe than under-frequency disturbance. Hence, deloading scheme 4 indicates the least standard frequency deviation. Obviously, participating in frequency regulation inevitably brings about wind power generation loss. The total captured wind energy with MPPT control is 1148.533 kWh. When the proposed control with deloading schemes 4, 3, 2 and 1, respectively, is implemented, the total captured wind energy decreases to 1086.496 kWh, 1075.825 kWh, 1055.470 kWh, and 1034.059 kWh, respectively. By comparison, the deloading scheme 1 has the minimum energy loss. According to Fig. 11(d), the proposed control leads to more rotor speed variations compared with the MPPT control, since KE stored in the rotational rotor is used to smooth frequency fluctuations. Similarly, as shown in Fig. 11(e), the blade pitch angle activates more frequently to provide frequency regulation support. In the situation where the wake effect is not considered, simulation results exhibit that the standard frequency deviation is 0.0873 and the total captured wind energy is 1477.548 kWh in MPPT control mode. These two parameters decrease to 0.0395 and 1350.614 kWh by means of the proposed control with deloading scheme 1. Similar to the constant wind speed scenarios, simulation results verify that the total power production and frequency regulation capability from WF are both over-estimated under time-varying wind speed conditions.

V. Conclusion

To facilitate frequency regulation in power systems, an adaptive frequency-responsive control framework for WFs considering wake interactions is proposed. The proposed framework holistically combines virtual inertia control and primary frequency control. The newly devised controller features online adjustable control gains. In addition, multiple primary reserve control approaches are developed, through which WTs can timely adjust the reserve and respond to both under-frequency and over-frequency events. Simulation results demonstrate that the frequency behavior is significantly improved by means of the proposed control strategy. Besides, by comparing different primary reserve control approaches, it can be concluded that: ① the improvement of frequency nadir/peak is proportional to the available charging/discharging range of KE; ② the reduction of quasi-steady-state frequency deviation is proportional to the available power reserve/curtailment capacity; ③ the manipulation of blade pitch angle of upstream WTs can reduce the power production loss induced by the wake effect; ④ there is a trade-off between the frequency regulation and total power generation. Overall, the results demonstrate that system operators should consider the wake model when assessing the frequency regulation capability from a WF. Future work is underway to investigate the optimal primary reserve capacity for a WF considering the trade-off between the frequency control performance and wind power maximization.

Appendix A

TABLE AI
Model Parameters of DFIG-based WTs

Item	Symbol	Value
Time constant of pitch serve	T	0.5 s
Inertia time constant	H	4 s
Nominal power	P_{nom}	5 MW
Terminal voltage	U_g	3.3 kV
Capacitance of DC-link capacitor	C	4813 μF
Rated DC-link voltage	$U_{dc,rated}$	1.15 kV
Lower limit of rotor speed	$\omega_{r,\min}$	0.7 p.u.
Upper limit of rotor speed	$\omega_{r,\max}$	1.22 p.u.
The maximum inertia control gain	$K_{in,\max}$	4
The maximum droop control gain	$K_{d,\max}$	40

TABLE AII
Model Parameters of SGs

Item	Symbol	Value
Nominal capacity	S_{g1}	120 MVA
Nominal capacity	S_{g2}	40 MVA
Terminal voltage	U_g	30 kV
Inertia time constant	H_{g1}	8.7 s
Inertia time constant	H_{g2}	4 s
Turbine permanent droop	R_P	0.04
Governor time constant	T_r	8.408 s
Servo-motor time constant	T_{servo}	0.5 s
Exciter regulator gain	K_{gain}	400
Exciter time constant	T_e	0.01 s

References

[1] S. Boubzizi, H. Abid, and M. Chaabane, "Comparative study of three types of controllers for DFIG in wind energy conversion system," *Protection and Control of Modern Power Systems*, vol. 3, no. 1, p. 21, Jul. 2018.
[2] Y. Yang, M. Bao, Y. Ding *et al*., "Impact of down spinning reserve on operation reliability of power systems," *Journal of Modern Power Systems and Clean Energy*, vol. 8, no. 4, pp. 709-718, Jul. 2020.
[3] W. Yan, X. Wang, W. Gao *et al*., "Electro-mechanical modeling of wind turbine and energy storage systems with enhanced inertial response," *Journal of Modern Power Systems and Clean Energy*, vol. 8, no. 5, pp. 820-830, Sept. 2020.
[4] X. Zhang, Y. Fu, S. Wang *et al*., "Effects of two-area variable inertia on transient stabilisation in interconnected power system with DFIG-based wind turbines," *IET Renewable Power Generation*, vol. 11, no. 5, pp. 696-706, Apr. 2017.
[5] R. Eriksson, N. Modig, and K. Elkington, "Synthetic inertia versus fast frequency response: a definition," *IET Renewable Power Generation*, vol. 12, no. 5, pp. 507-514, Apr. 2017.
[6] C. Pradhan, C. N. Bhende, and A. K. Samanta, "Adaptive virtual inertia-based frequency regulation in wind power systems," *Renewable energy*, vol. 115, pp. 558-574, Jan. 2018.

[7] M. H. Ravanji, C. A. Canizares, and M. Parniani, "Modeling and control of variable speed wind tur-bine generators for frequency regulation," *IEEE Transactions on Sustainable Energy*, vol. 10, no. 2, Apr. 2019.
[8] M. Hwang, E. Muljadi, J.-W. Park *et al*., "Dynamic droop-based inertial control of a doubly-fed induction generator," *IEEE Transactions on Sustainable Energy*, vol. 7, no. 3, pp. 924-933, Jul. 2016.
[9] S. Ghosh, S. Kamalasadan, N. Senroy *et al*., "Doubly fed induction generator (DFIG)-based wind farm control framework for primary frequency and inertial response application," *IEEE Transactions on Power Systems*, vol. 31, no. 3, pp. 1861-1871, May 2015.
[10] K. Vidyanandan and N. Senroy, "Primary frequency regulation by deloaded wind turbines using variable droop," *IEEE transactions on Power Systems*, vol. 28, no. 2, pp. 837-846, May 2012.
[11] H. Ye, W. Pei, and Z. Qi, "Analytical modeling of inertial and droop responses from a wind farm for short-term frequency regulation in power systems," *IEEE Transactions on Power Systems*, vol. 31, no. 5, pp. 3414-3423, Sept. 2015.
[12] E. Jahan, M. R. Hazari, S. Muyeen *et al*., "Primary frequency regulation of the hybrid power system by deloaded PMSG-based offshore wind farm using centralised droop controller," *The Journal of Engineering*, vol. 2019, no. 18, pp. 4950-4954, Jul. 2019.
[13] P. Li, W. Hu, R. Hu *et al*., "Strategy for wind power plant contribution to frequency control under variable wind speed," *Renewable energy*, vol. 130, pp. 1226-1236, Jan. 2019.
[14] S. Wang and K. Tomsovic, "A novel active power control framework for wind turbine generators to improve frequency response," *IEEE Transactions on Power Systems*, vol. 33, no. 6, pp. 6579-6589, Nov. 2018.
[15] X. Tang, M. Yin, C. Shen *et al*., "Active power control of wind turbine generators via coordinated rotor speed and pitch angle regulation," *IEEE Transactions on Sustainable Energy*, vol. 10, no. 2, pp. 822-832, Apr. 2018.
[16] M. G. Simões and A. Bubshait, "Frequency support of smart grid using fuzzy logic-based controller for wind energy systems," *Energies*, vol. 12, no. 8, p. 1550, Apr. 2019.
[17] S. Kuenzel, L. P. Kunjumuhammed, B. C. Pal *et al*., "Impact of wakes on wind farm inertial response," *IEEE Transactions on Sustainable Energy*, vol. 5, no. 1, pp. 237-245, Jan. 2014.
[18] J. Lee, E. Muljadi, P. Srensen *et al*., "Releasable kinetic energy-based inertial control of a DFIG wind power plant," *IEEE Transactions on Sustainable Energy*, vol. 7, no. 1, pp. 279-288, Jan. 2016.
[19] A. de Paola, D. Angeli, and G. Strbac, "Scheduling of wind farms for optimal frequency response and energy recovery," *IEEE Transactions on Control Systems Technology*, vol. 24, no. 5, pp. 1764-1778, Sept. 2016.
[20] X. Lyu, Y. Jia, and Z. Xu, "A novel control strategy for wind farm active power regulation considering wake interaction," *IEEE Transactions on Sustainable Energy*, vol. 11, no. 2, pp. 618-628, Apr. 2020.
[21] S. Ma, H. Geng, G. Yang *et al*., "Clustering-based coordinated control of large-scale wind farm for power system frequency support," *IEEE Transactions on Sustainable Energy*, vol. 9, no. 4, pp. 1555-1564, Oct. 2018.
[22] A. S. Ahmadyar and G. Verbič, "Coordinated operation strategy of wind farms for frequency control by exploring wake interaction," *IEEE Transactions on Sustainable Energy*, vol. 8, no. 1, pp. 230-238, Jan. 2016.
[23] M. Kayikçi and J. V. Milanovic, "Dynamic contribution of DFIG-based wind plants to system frequency disturbances," *IEEE Transactions on Power Systems*, vol. 24, no. 2, pp. 859-867, May 2009.
[24] R. G. de Almeida, E. D. Castronuovo, and J. P. Lopes, "Optimum generation control in wind parks when carrying out system operator requests," *IEEE Transactions on Power Systems*, vol. 21, no. 2, pp. 718-725, May 2006.
[25] J. F. Ainslie, "Calculating the flowfield in the wake of wind turbines," *Journal of Wind Engineering and Industrial Aerodynamics*, vol. 27, no. 3, pp. 213-224, Jan. 1988.
[26] R. J. Barthelmie, "Comparison of wake model simulations with offshore wind turbine wake profiles measured by sodar," *Journal of Atmospheric and Oceanic Technology*, vol. 23, no. 7, pp. 888-901, Jul. 2006.
[27] N. O. Jensen. (1983, May). A note on wind generator interaction. [Online]. Available: http://citeseerx. ist. psu. edu/viewdoc/download? doi= 10.1.1.456.4080&rep=rep1&type=pdf
[28] IEEE. (1992, Aug.) Recommended practice for functional and performance characteristics of control systems for steam turbine-generator units. [Online]. Available: https://ieeexplore-ieee-org.eproxy.lib.hku.hk/stamp/stamp.jsp?tp=&arnumber=159442

Xue Lyu received the B.Eng. degree from Qingdao University of Technology, Qingdao, China, in 2013, the M. Eng. degree from Shanghai University of Electric Power, Shanghai, China, in 2016, and the Ph.D. degree from The Hong Kong Polytechnic University, Hong Kong, China, in 2019. She is now a Postdoctoral Fellow at the University of Hong Kong, Hong Kong, China. She is also a Visiting Scholar in the Department of Electrical and Electronic Engineering, Southern University of Science and Technology, Shenzhen, China. Her research interests include modeling and control for grid-integration of renewable energy systems.

Youwei Jia received the B.Eng. and Ph.D. degrees from Sichuan University, Chengdu, China, in 2011, and The Hong Kong Polytechnic University, Hong Kong, China, in 2015, respectively. From 2015 to 2018, he was a Postdoctoral Fellow at The Hong Kong Polytechnic University. He is currently an Assistant Professor with the Department of Electrical and Electronic Engineering, Southern University of Science and Technology, Shenzhen, China. His research interests include microgrid, renewable energy modeling and control, power system security analysis, complex network and artificial intelligence in power engineering.

Zhao Yang Dong received the Ph.D. degree in electrical engineering from the University of Sydney, Sydney, Australia, in 1999. He is currently with the University of New South Wales, Sydney, Australia. His previous roles include the Ausgrid Chair and the Director of Ausgrid Centre for Intelligent Electricity Networks; a Professor and the Head of School of Electrical and Information Engineering, University of Sydney; a Manager of System Planning with Transend Networks (currently, TASNetworks), Lenah Valley, Australia. His research interests include power system planning, smart grid/microgrid, power system stability assessment, load modeling, and computational methods.